Journal of Materials Chemistry A

COMMUNICATION

View Article Online
View Journal | View Issue

Cite this: J. Mater. Chem. A, 2014, 2, 20486

Received 14th September 2014
Accepted 22nd October 2014

DOI: 10.1039/c4ta04807e

www.rsc.org/MaterialsA

Facile preparation of MnO_2 doped Fe_2O_3 hollow nanofibers for low temperature SCR of NO with NH_3†

Sihui Zhan,*[a] Mingying Qiu,*[a] Shanshan Yang,[a] Dandan Zhu,[a] Hongbing Yu[a] and Yi Li*[b]

A series of MnO_2 doped Fe_2O_3 hollow nanofibers with different Mn/Fe molar ratios were successfully synthesized by the electrospinning method for the low temperature selective catalytic reduction (SCR) of NO with NH_3 in the presence of excess O_2. The SEM and TEM images showed obvious hollow tubular structure of electrospun nanofibers. The hollow nanofibers with Mn/Fe molar ratio of 0.15 exhibited the highest catalytic activity, nearly 100% of NO conversion from 150 to 300 °C, among the catalysts investigated. The TPR, XPS and *in situ* FTIR results revealed that Mn^{4+} was the main active species for SCR reaction, and the addition of Mn species enhanced the surface concentration and acidity of Lewis acid sites.

1. Introduction

Nitrogen oxides (NO_x) from industrial flue gas have been leading to more and more environmental problems, including photochemical smog, acid rain and ozone depletion.[1–4] To date, selective catalytic reduction (SCR) of NO_x with NH_3 is the most effective technology for removing NO_x,[5,6] and commercial V_2O_5–WO_3/TiO_2 catalysts have been widely used for the removal of NO_x from stationary sources.[7–11] However, there are some drawbacks of V_2O_5–WO_3/TiO_2 catalysts, such as high cost, the toxicity of vanadium species and narrow temperature window of 300–400 °C.[12] Therefore, it is necessary to develop novel low-temperature SCR catalysts, which can be set down to downstream of a desulfurization scrubber or a particulate control device, in order to avoid deactivation and save energy.[13,14]

Previous studies have showed that mixed transition metal oxides, including Cu, Fe, Co, Mn, Ce, Cr, and Ni, have the advantages of good low-temperature SCR activity and low cost. Among these, manganese and iron oxides are attracting considerable attention because of their high SCR activity at low temperature, low cost, and non-toxicity.[15–20] However, these Fe-base catalysts were usually prepared with the impregnation approach and were prone to be easily deactivated by SO_2 present in the treated flue gas. Therefore, the stability of catalytic activity, sulfur tolerance, and water resistance should be enhanced by formulation modification and structure adjustment.

In the past few years, various methods have been used to synthesize nanoparticles, including hydrothermal,[20–23] sol–gel,[24] and co-precipitation methods.[25] However, in catalytic processes, pore diffusion resistance is an obvious issue for nanoparticles, which is hard to handle and usually causes several serious problems of high pressure drop in industrial applications.[26] To overcome these disadvantages, electrospinning is applied for synthesizing hollow nanofibers or tubules, which have attracted considerable attention for their hierarchical tubules-within-a-tubule structure, as well as fibrous mat structure, large surface area and sufficient mechanical integrity. Just because of these advantages, the long hollow fibers could act as a micro-reactor and could be packed or constructed in the best form to fit the particular application in several fields such as energy storage, semiconductors and gas sensors.[27–29] However, to the best of our knowledge, there is no report on using electrospun nanofibers as an SCR catalyst to remove NO_x with NH_3.

In this paper, manganese doped iron-based hollow nanofibers were successfully synthesized by electrospinning the corresponding precursor and calcination. The activities for the low temperature SCR of NO with NH_3 in the presence of excess O_2 at the relatively high space velocity of 50 000 h^{-1} were investigated. The hollow nanofibers with a Mn/Fe molar ratio of 0.15 exhibited an excellent NO_x SCR performance of complete NO reduction at as low as 150 °C, which can be attributed to its relatively high surface area, high surface Mn^{4+} concentration,

[a]College of Environmental Science and Engineering, Key Laboratory of Environmental Pollution Process and Environmental Criteria, Nankai University, Tianjin 300071, P. R. China. E-mail: sihuizhan@nankai.edu.cn; jkcs66902@163.com; Fax: +86-22-23502756; Tel: +86-22-23502756

[b]Department of Chemistry, Tianjin University, Tianjin 300072, P. R. China. E-mail: liyi@tju.edu.cn

† Electronic supplementary information (ESI) available. See DOI: 10.1039/c4ta04807e

and the high concentration of Lewis acid sites, as characterized by BET, XPS, TPR, and *in situ* FTIR.

2. Experimental section

2.1. Catalyst preparation

All the chemicals used were of analytical grade. Citric acid, ferric citrate and manganese acetate were purchased from Sinopharm chemical reagent company without further purification.

In a typical process, 0.03 mol of citric acid and 0.01 mol of ferric citrate were dissolved in 50 mL deionized water with magnetic stirring for 3 h, which was then filtered to remove insoluble contaminants to obtain a transparent solution A. Moreover, 0.001 mol manganese acetate was dissolved in 5 mL deionized water in order to obtain a solution B. After being completely dissolved, solution B was poured into solution A with magnetic stirring for 30 min at room temperature, and then the mixed solution was aged at 60 °C for 24 h at 4–5 Pa s.

In a typical electrospinning process, the spinnable sol was transferred into a plastic injector, and the sol was pressurized with a syringe pump (Cole-Parmer 74900-05, USA). The metallic needle was connected to a high-voltage supply (DW-P503-4ACCD, Tianjin, China), and a piece of stainless steel board was used to collect the gel fibers. All the experiments were conducted at room temperature, the applied voltage was 15 kV, and the distance between the spinneret and the collector was 10 cm. Finally, the xerogel fibers were calcined at 400 °C for 4 h in air at a heating rate of 0.5 °C min^{-1} to obtain the desired products. The hollow nanofibers were denoted as MnFe (x) ("x" represented the MnO_x/Fe_2O_3 molar ratio; $x = 0$, 0.01, 0.05, 0.10, 0.15, 0.20). All the above catalysts were ground and sieved to 40–60 mesh for further measurements.

2.2. Catalyst characterization

The morphology and structure of the fibers were analysed using a scanning electron microscope (SEM, Shimadzu SS-550) and a high-resolution transmission electron microscope (HRTEM, Tecnai G2F20). The X-ray diffraction (XRD) patterns of samples were recorded *via* an X-ray diffractometer (Rigaku D/Max 2200PC) with a graphite monochrometer and CuKα radiation ($\lambda = 0.15418$ nm) in the range of 20–80°. The voltage and current were 40 kV and 40 mA, respectively. The Fourier transform infrared (FTIR) spectra were recorded on a Nicolet 5DX-FTIR spectrometer using the KBr pellet method in the range of 400–4000 cm^{-1}. N_2 adsorption–desorption data were obtained using a Quantachrome SI Micromeritics apparatus. X-ray photoelectron spectroscopy (XPS) spectra were collected on an ESCALAB 250 multi-technique X-ray photoelectron spectrometer (UK) using a monochromatic AlKα X-ray source ($h\nu = 1486.6$ eV). All the XPS spectra were recorded using an aperture slot of 300 × 700 microns, survey spectra were recorded with a pass energy of 160 eV, and high resolution spectra with a pass energy of 40 eV. Temperature-programmed reduction (H_2-TPR) experiments were conducted on a Micromeritics ChemiSorb 2720 instrument using approximately 20 mg of samples. The samples were pretreated at 300 °C for 1 h under a N_2 flow. The temperature was linearly increased from 50 to 1000 °C at 10 °C min^{-1} while H_2 consumption was continuously recorded. The *in situ* DRIFTS spectra were recorded with on an AVATAR 370 Fourier transform infrared spectrometer. Prior to each experiment, the sample was heated to 350 °C in He for 1 h, and then cooled to 150 °C. The spectra were recorded by accumulating 32 scans at a resolution of 4 cm^{-1}.

2.3. SCR activity measurements

The catalytic activities were evaluated using a bench-scale experimental system. In each test, hollow fibrous catalyst was loaded in a temperature controlled fixed-bed quartz flow reactor (i.d. 20 mm) containing 0.5 g of catalyst to control the reaction temperature. All the individual flue gas components were precisely controlled by mass flow controllers (MFC), with a total flow rate of 300 mL min^{-1} (refers to 1 atm and 298 K), which corresponded to a gas hourly space velocity (GHSV) of 50 000 h^{-1}. The typical composition of the initial reactant gas was 500 ppm NO, 500 ppm NH_3, 5 vol% O_2, and balance N_2. The NO, NH_3, NO_2 and N_2O concentrations at both the inlet and outlet of the reactor were measured online by a FTIR spectrometer (Gasmet FTIR DX4000, Finland). The reaction system was maintained for 1 h at each reaction temperature to reach a steady state before the analysis of the catalyst was performed. The NO_x conversion was calculated as follows:

$$\text{NO conversion (\%)} = 100\% \times (1 - [NO_x]_{out}/[NO_x]_{in})$$

$$N_2 \text{ selectivity (\%)} = 100\% \times \{1 - ([NO_2]_{out} + 2[N_2O]_{out})/([NO_x]_{in} + [NH_3]_{in} - [NH_3]_{out})\}$$

where $[NO_x] = [NO] + [NO_2]$, and the subscripts "in" and "out" indicate the inlet concentration and outlet concentration at steady state, respectively.

3. Results and discussion

3.1. Characteristics

To obtain structural information of the MnFe composite hollow nanofibers, XRD patterns were obtained and are shown in Fig. 1. There were five diffraction peaks at 31.28°, 35.08°, 43.18°, 56.58° and 62.88°, which belonged to magnetite Fe_2O_3 (PDF#19-0629). With increasing manganese content, the diffraction peak of Fe_2O_3 became lower and lower, indicating its composed nanoparticles became larger and larger.[30,31] However, no visible phase of Mn species could be observed, this may be due to the fact that MnO_x was well incorporated into the matrix of Fe_2O_3 or that the Mn oxides were in a highly dispersed state or the crystallites formed were less than 5 nm beyond the detection limitation. Furthermore, the full width at half-maximum (fwhm) of the peaks for MnFe (x = 0.01–0.2) were lower compared to Fe_2O_3, indicating that the grain size of Fe_2O_3 on MnFe (x = 0.01–0.2) was smaller compared to Fe_2O_3. This indicated that the existence of MnO_x could lower the crystallinity of Fe_2O_3, and thus enhance the dispersion of Fe_2O_3 on the catalyst surface.

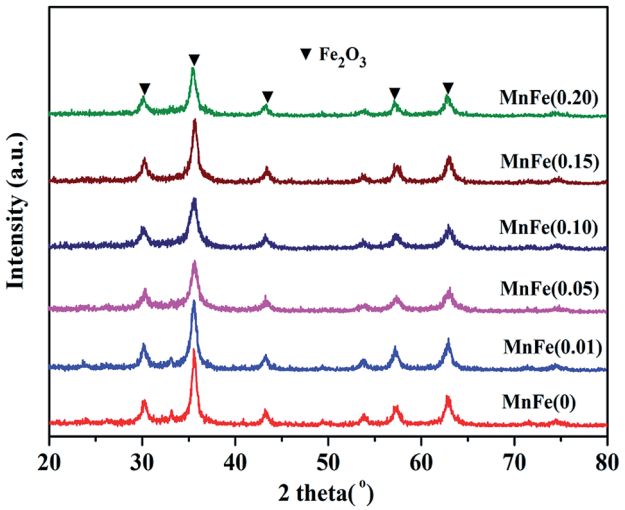

Fig. 1 XRD patterns of MnFe hollow nanofibers.

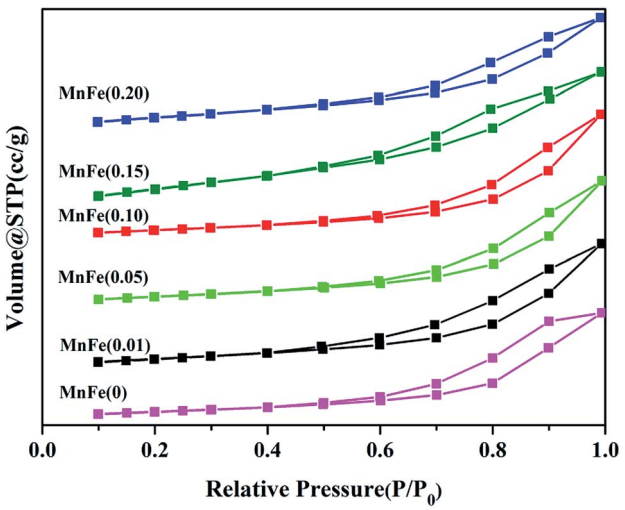

Fig. 2 Nitrogen adsorption isotherms of MnFe nanofibers.

Table 1 The specific area, pore volume and pore diameter distribution of MnFe nanofibers

Materials	Specific area ($m^2\ g^{-1}$)	Pore volume ($cm^3\ g^{-1}$)	Pore diameter (nm)
Fe_2O_3	96.5	0.29	8.8
MnFe (0.01)	102.2	0.29	8.8
MnFe (0.05)	108.2	0.26	8.8
MnFe (0.10)	112.8	0.30	6.1
MnFe (0.15)	137.1	0.35	6.6
MnFe (0.20)	124.4	0.27	6.8

The N_2 adsorption–desorption isotherms are shown in Fig. 2, and data of pore size distribution, pore volume, and surface area are listed in Table 1. From Fig. 2, all MnFe (x) hollow nanofibers with different Mn/Fe mole ratio showed typical IV curves and H1 type hysteresis loop, indicating that the formation of the mesoporous structure.[4,32] Upon increasing the Mn doping content, the surface area improved from 96.5 to 137.1 $m^2\ g^{-1}$ (Table 1). Moreover, the higher manganese loading enhanced NO conversion until the mole ratio of MnO_x/Fe_2O_3 reached 0.15. Beyond this value, a further increase of manganese loading could lead to sintering or the collapsing of the structure, which was harmful to the BET surface and catalytic activity. It is implied that the low-temperature reduction activity of NO_x is related to the apparent surface properties to some extent. As shown in Table 1 and Fig. 6, both the BET surface (124.4 $m^2\ g^{-1}$) and the low temperature activity of MnFe (0.20) catalyst were lower compared to MnFe (0.15). This phenomenon is also verified by scanning electron microscopy (SEM) images of these catalysts (Fig. 3a–c).

3.2. SEM and TEM analysis

Fig. 3 shows typical scanning electron microscopy (SEM) and transmission electron microscopy (TEM) images of the as-prepared MnFe hollow nanofibers. From Fig. S1,† it can be seen that the MnFe (0.05) nanofibers had a hollow structure but a non-uniform size. As to MnFe (0.20) (Fig. S2†), the hollow structure is partially incomplete and collapsed, and the result was consistent with the conclusion derived from N_2 adsorption–desorption isotherm data. As shown in Fig. 3c, all of MnFe (0.15) nanofibers had a hollow structure and were quite uniform in cross-section, and there were almost 60% of hollow nanofibers with outer diameter from 50 nm to 200 nm. The change of outer diameter should be attributed to the gradual loss of citrate agents from the nanofibers and the crystallisation of Fe_2O_3. After calcinations, the hollow MnFe (0.15) nanostructured fibers were smooth and composed of numerous nanoparticles with a relatively uniform distribution of typically 5–20 μm long and having larger coarser surfaces, which provided a larger accessible surface area between the gas molecules and catalyst. Fig. 3b clearly indicated that the uniform tubular structure with an outer diameter of 312 nm and a 10 nm wall thickness. TEM and HRTEM were also used to check the microstructure of the MnFe (0.15) catalyst. As shown in Fig. 3a, a typical hollow tubular structure with an average outer diameter of about 140 nm and a uniform wall thickness could be observed easily. Moreover, high-resolution transmission electron microscopy (HRTEM) was used to characterize the lattice structure. The two different lattice fringes can be clearly observed in Fig. 3d, one was around 0.361 nm, which matched with Fe_2O_3 (0.361 nm) in plane (011) and the other was 0.293 nm, corresponding to Fe_2O_3 (0.295 nm) in (110) or manganese oxides (0.291 nm) in (201).[20,33] These results indicate that the synthesized hollow fibers have good crystallinity and provide a large accessible surface area.

The possible mechanism of formation of electrospun hollow nanofibers is as following: after electrospinning the xerogel nanofibers, a rigid outer shell was formed. However, it was still fluid in the center of the fibers at that time, and a large amount of solvent and citric acid anions remained in the gel fibers. When the gel fiber was calcined in a tubular furnace, the sol particles diffused to the inner surface of the outer shell with the evaporation of the organic compounds, and thus the novel

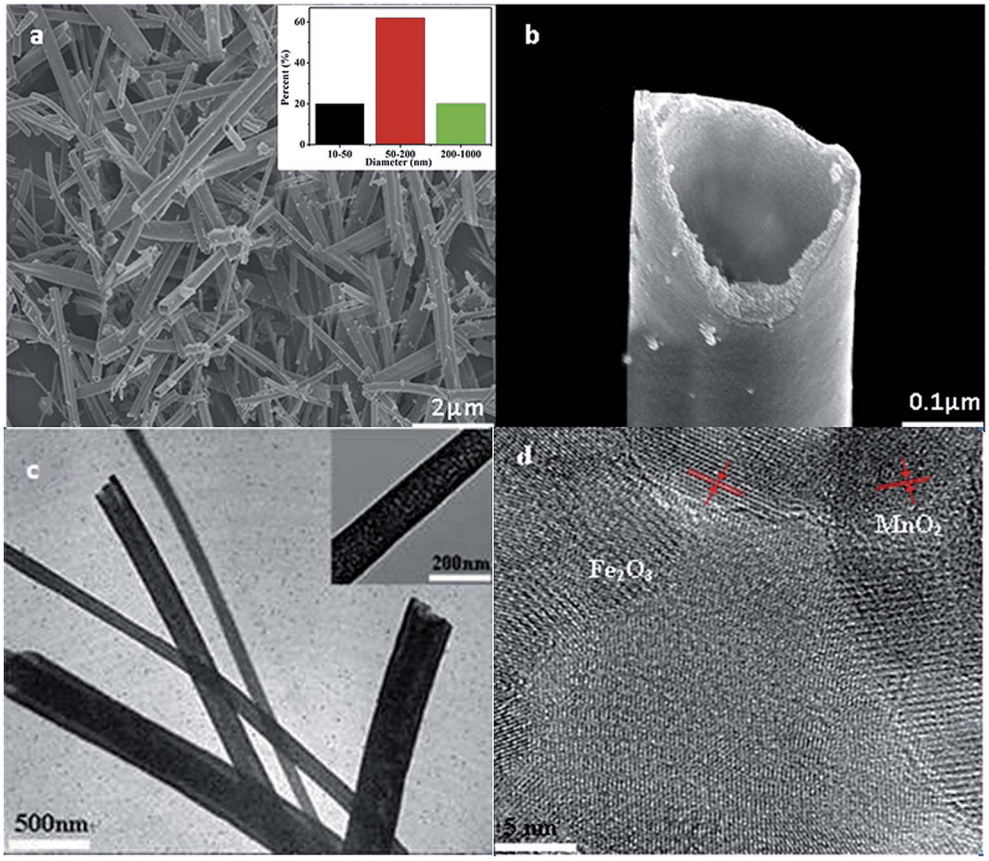

Fig. 3 (a) SEM image of electrospun MnFe (0.15) hollow nanofibers (inset: the pore size distribution); (b) SEM image of the cross-section; (c) TEM image of MnFe (0.15) hollow nanofibers (inset: under high magnification); (d) HRTEM image of MnFe (0.15) hollow nanofibers.

tubular structure was first formed. Even at this stage, there were still several organic parts remaining in the fibers. Upon increasing the heating temperature, citrate anions began to decompose to produce CO_2 and H_2O gases, which went out of the fibers through the tube, and a crystallized hollow fiber was formed.[34]

3.3. H_2-TPR and XPS analysis

H_2-TPR is a widely used technique to investigate the redox properties of a catalyst. The H_2-TPR profiles of Fe_2O_3, MnFe (0.05), and MnFe (0.15) catalysts are illustrated in Fig. 4. All H_2 consumption peaks could be attributed to the reduction of iron, manganese species, and their reduction behavior was very different. For the Fe_2O_3 sample, there were two peaks across 250–550 °C and 600–800 °C, which corresponds to the following reduction steps: Fe_2O_3–Fe_3O_4 (327 °C) and Fe_3O_4–FeO (619 °C), respectively.[35,36] It can be seen from this figure that the peak positions shifted to higher temperatures after the introduction of manganese. The peak from 300 °C to 400 °C can be attributed to the combined reduction of Fe^{3+} and Mn^{3+} (or Mn^{4+}) with a structural transformation from $Fe_{2-y}Mn_yO_3$ to $(Fe–Mn)_3O_4$.[24,37] For these catalysts, there is likely to be a stronger metal–support interaction, thereby making it more difficult to carry out the reduction. For the MnFe (0.15) sample, increasing Mn loading decreases the temperature required for the reduction of Fe_3O_4–

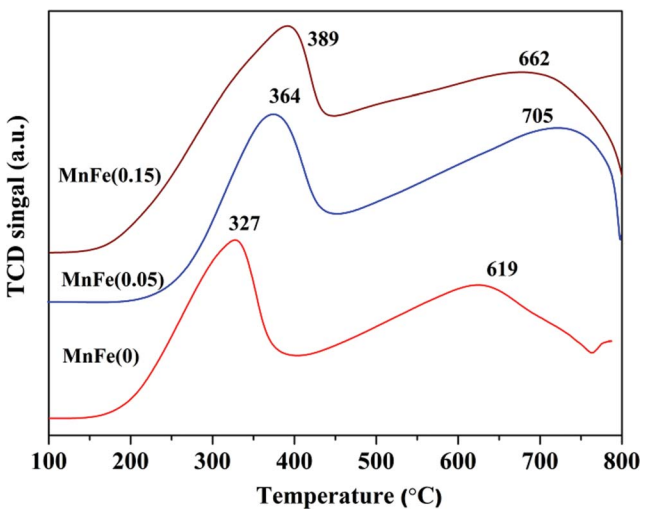

Fig. 4 H_2-TPR profiles of MnFe hollow nanofibers.

FeO (662 °C) compared to the MnFe (0.05) sample (705 °C), it is suggested that the mobility of surface oxygen was enhanced after the addition of Mn, and therefore there was more chemisorbed oxygen formed on the catalyst surface.[38]

In order to understand the nature of the interaction between the two metal oxide species, the oxidation states of Fe $2p_{3/2}$, Mn

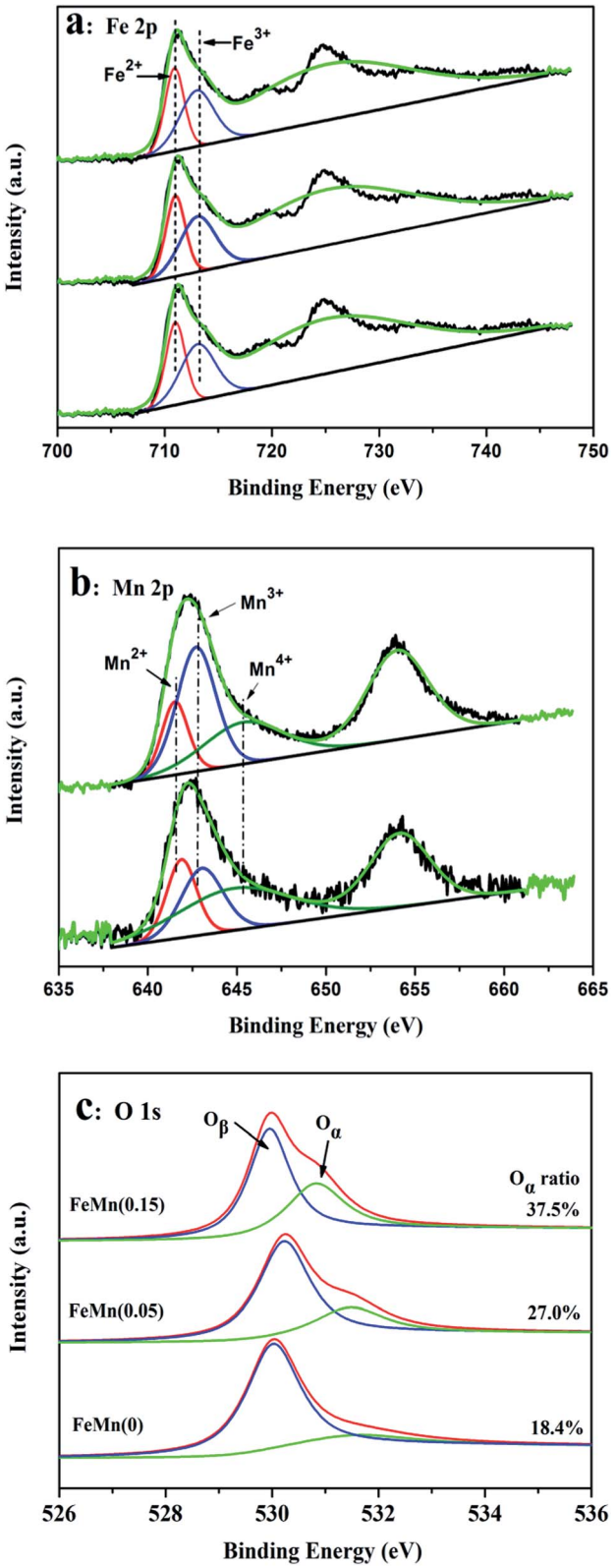

Fig. 5 (a) Fe 2p, (b) Mn 2p and (c) O 1s from XPS spectra of MnFe nanofibers.

$2p_{3/2}$, and O 1s in MnFe hollow nanofibers were detected by XPS as shown in Fig. 5. These spectra have been calibrated against the C ls peak standardized at 284.6 eV. As shown in Fig. 5a, the Fe $2p_{3/2}$ peak is separated into two peaks by the same peak fitting deconvolution technique. The peaks at 711.0 and 713.1 eV can be assigned to Fe^{2+} and Fe^{3+}, respectively.[19] The ratios of Fe^{2+}/Fe^{3+} on the surface of MnFe (0), MnFe (0.05) and MnFe (0.15) were approximately 0.80, 0.82 and 0.83, respectively, indicating that the increasing content of Mn increased with the content of Fe^{2+}, which required higher reduction temperature than Fe^{3+}.

As shown in Fig. 5b, two main peaks due to Mn $2p_{3/2}$ and Mn $2p_{1/2}$ can be observed from 642.5 eV to 653.9 eV. By performing a peak-fitting deconvolution, the Mn $2p_{3/2}$ spectra were separated into three peaks, Mn^{3+} (641.5–641.8 eV), Mn^{4+} (642.7–643.1 eV) and Mn nitrate (644.8–645.2 eV).[39] It could be clearly seen that the intensities of Mn^{4+} characteristic peaks increased with the addition of Mn, accompanied with a decrease of Mn^{3+} peaks. The ratios of Mn^{4+}/Mn^{3+} on the surface of MnFe (0.05) and MnFe (0.15) were approximately 1.2 and 2.5, respectively. Furthermore, the surface atom concentrations of Mn, Fe, and O and the atomic ratios of Mn/Fe are summarized in Table 2, the percent of O 1s on MnFe (0.15) fibers obviously increased with the increased Mn content. These species were sure to increase the activity of NO oxidation to NO_2, and thereby enhance the "fast SCR" reaction activity ($4NH_3 + 2NO + 2NO_2 \rightarrow 4N_2 + 6H_2O$).[40] The O 1s spectrum in Fig. 5c could be decomposed into two peaks, corresponding to various oxygen containing chemical bonds. According to the literature, the sub-bands at lower binding energy (530.0–530.4 eV) correspond to the lattice oxygen (denoted as O_β), and the sub-bands at higher binding energy (532.2–532.5 eV) correspond to the surface adsorbed oxygen (denoted as O_α), such as O_2^{2-} or O^- belong to defect oxide or hydroxyl-like groups.[22,41] As listed in Table 2, with the increasing of Mn doping, the chemisorbed oxygen O_α content was gradually increased, such that the ratios of $O_\alpha/(O_\alpha + O_\beta)$ over Fe_2O_3, MnFe (0.05) and MnFe (0.15) nanofibers were 18.4%, 27.0% and 37.5%, respectively. This may be related to the presence of the Mn^{3+} species, which could create a charge imbalance, vacancies, and unsaturated chemical bonds on the catalyst surface, and would lead to the increase in oxide defects or hydroxyl-like groups. As know, surface chemisorbed oxygen is thought to be the most active oxygen and plays an important role in oxidation reactions. This indicate that the MnFe (0.15) nanofibers might have better activity for the oxidation of NO to NO_2 compared to pure Fe_2O_3 in the NH_3-SCR process.

3.4. Low-temperature catalytic performance

The NO_x conversions, N_2 selectivities, and N_2O formations of the Mn–Fe catalysts with different molar ratios of Fe/Mn are

Table 2 XPS results of various catalysts

	Surface atomic concentration (%)				
Hollow fibers	Fe	Mn	O_α	O_β	O_{total}
Fe_2O_3	29.3	0	13.01	57.69	70.7
MnFe (0.05)	24.41	2.48	19.74	53.37	73.11
MnFe (0.15)	17.95	6.47	28.34	47.74	75.58

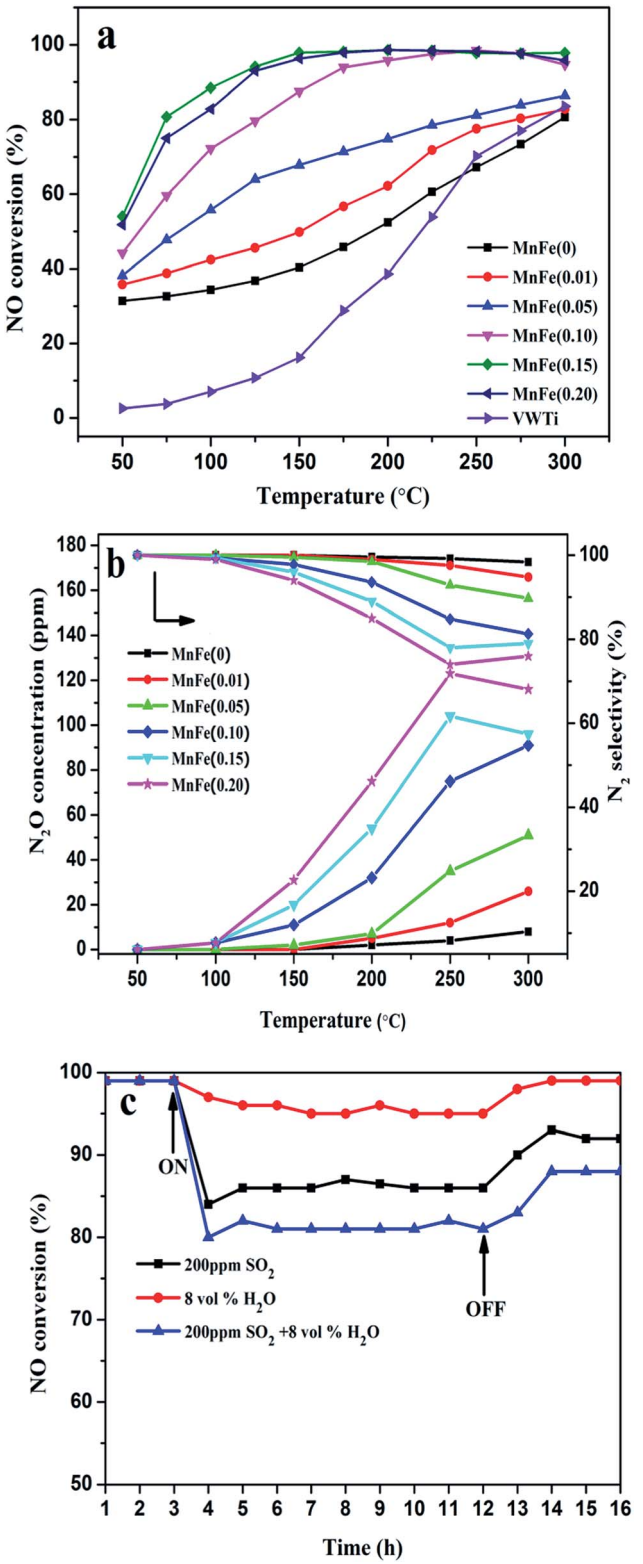

Fig. 6 (a) NO_x conversion using MnFe (x) hollow fibrous catalyst and VWTi catalyst; (b) N_2 selectivity and N_2O concentration in the SCR reaction; (c) influence of H_2O and SO_2 on NO conversion in the SCR reaction over MnFe (0.15) catalyst at 150 °C. Reaction conditions: [NO] = 500 ppm, [NH_3] = 500 ppm, [SO_2] = 200 ppm, [H_2O] = 8%, [O_2] = 5%, GHSV = 50 000 h^{-1}.

shown in Fig. 6. Experimental results show that there was only 38–80% NO_x conversion when pure Fe_2O_3 was used as SCR catalyst at 100–300 °C, and the addition of Mn content could significantly increase NO_x conversion below 250 °C. It was found that the NO_x conversion was greatly improved from 38% to 100% with an increase in the Mn/Fe molar ratio from 0 to 0.2 at 150 °C, the N_2 selectivity decreased with an increase in Mn/Fe molar ratio (as shown in Fig. 6b). For the MnFe (0.15) catalyst, the NO_x conversion was approximately 100% at 150 °C, and the amount of N_2O formed was below 20 ppm at 150 °C, indicating its promising N_2 selectivity.

The influences of 200 ppm SO_2 and 8 vol% H_2O on the performance of the MnFe (0.15) catalyst were investigated at 150 °C and the results are illustrated in Fig. 6c. It could be seen that a slight NO conversion decline occurred when 200 ppm SO_2 was added, and then became stable, and after removing SO_2 the conversion recovered to 92%. When 8 vol% H_2O was introduced into the stream, the NO conversion declined and remained at about 96%, and after stopping H_2O the conversion restored to 99%. When the 200 ppm SO_2 and 8 vol% H_2O were injected into the feed gases at the same time, NO conversion decreased a little more, but the NO conversion still maintained at about 82%. The above results suggested that the catalyst had certain SO_2/H_2O durability.

3.5. *In situ* FTIR analysis

To investigate the reaction mechanism in detail, the *in situ* DRIFTS experiment of reaction between NH_3 and pre-adsorbed NO + O_2 species at 150 °C was carried out and the results are shown in Fig. 7. In this experiment, the hollow nanofibers was first treated with NO + O_2/Ar for 1 h, and then purged with Ar for 30 min. When NH_3 was introduced at 150 °C, the DRIFT spectra could be recorded as a function of time (Fig. 7a). After NH_3 passed over the NO + O_2 pretreated catalyst, the band at 1610 cm^{-1} due to NO_2 (ref. 41) decreased and after 1 min, the bidentate nitrate species (1580 cm^{-1})[30] on manganese oxides gradually disappear. After NH_3 was introduced for 10 min, the band at 1580 cm^{-1} disappeared, indicating that bidentate nitrate had participated in the reaction process, the band at 1550 cm^{-1} appeared, which could be assigned to the intermediate of the oxidation of ammonia.[42,43] As already noted, the intensity of the band at 1240 cm^{-1} due to bridged nitrate obviously increases, and its position shifted to 1260 cm^{-1}, which could be ascribed to the deformation of the nitrate species.[44] Moreover, the IR bands attributed to coordinated NH_3 (1260 and 1602 cm^{-1}) on the Lewis acid sites, ionic NH_4^+ (1440 cm^{-1}) on Brønsted-acid sites appeared, and the bands in the region of 3700–3000 cm^{-1} attributed to N–H stretching vibration could also observed.[45] After the catalyst was purged with NH_3 for 10 min, both adsorbed NH_3 and NO_x species could be observed on the catalyst surface. These results indicated that only the reaction between NO_2 and ammonia had occurred. Furthermore, the coexistence of ammonia and nitrate species showed that NH_3 and NO_x could be adsorbed over different active sites of the catalyst surface.

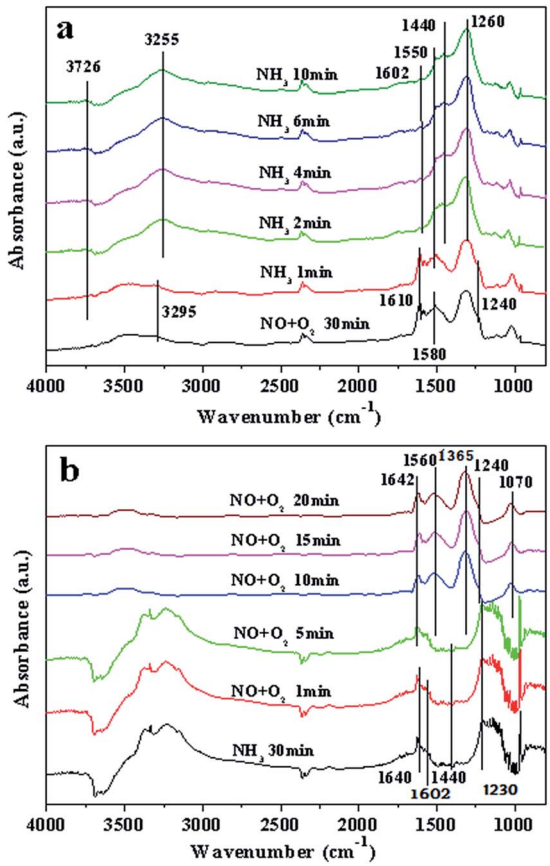

Fig. 7 *In situ* DRIFT spectra of MnFe (0.15) catalyst for the reaction between (a) NH_3 and adsorbed NO_x at 150 °C, (b) NO + O_2 and adsorbed NH_3 species at 150 °C.

In this experiment, the reactants were introduced to the MnFe (0.15) catalyst in the reversed order (as shown in Fig. 7b). After the MnFe (0.15) catalyst was first purged with NH_3 for 30 min, the catalyst surface was mainly covered by coordinated NH_3 (1207, 1230, 1440, 1602 and 1640 cm^{-1}).[45] When NO + O_2 was introduced for 2 min, the bands due to adsorbed NH_3 species slightly decrease and totally disappear after 10 min. At the same time, the nitrate species began to form on the catalyst surface. However, bands at 1560 cm^{-1} increased a bit, which could also prove the oxidation of ammonia such as nitrate or nitrite.[41] After the catalyst was purged with NO + O_2 for 20 min, the catalyst surface was mainly covered by monodentate nitrate (1365 cm^{-1} and 1560 cm^{-1}).[30,46] On the basis of the above results, it can be concluded that coordinate NH_3 played important roles in reducing NO_x in SCR reaction.

In general, when the SCR reaction happened at 150 °C, both adsorbed NH_3 and NO_x species were considered to be involved in the SCR reaction. In addition, the coordinated NH_3, as well as *in situ* formed NO_2 species were considered to be involved in the NH_3-SCR reaction following an L–H mechanism.[47,48]

4. Conclusions

In this paper, hollow MnFe nanofibers with different Mn doping content were prepared by the electrospinning method, which were highly active for the low temperature selective catalytic reduction (SCR) of NO with NH_3. The MnFe (0.15) hollow fibers showed the highest activity and 100% NO_x conversion at 150 °C with a space velocity of 50 000 h^{-1}. In addition, the large BET surface areas present in the catalyst also contributed to facilitate the SCR reaction. On the basis of the *in situ* DFTIR analysis, high surface acidity, the formation of the intermediate, and the better low temperature reducibility properties, would be the main reasons for the high low-temperature catalytic activity.

Acknowledgements

The authors gratefully acknowledge the financial support of national natural foundation of china (21377061), Asia Research Center in Nankai University (AS1326), Natural Science Foundation of Tianjin (12JCQNJC05800), Key Technologies R&D Program of Tianjin (13ZCZDSF00300) and the assistance of Dr Raymond Seekell (University of Notre Dame) in manuscript preparation and discussion.

Notes and references

1 K. Mathisen, D. G. Nicholson and A. N. Fitch, *J. Mater. Chem.*, 2005, **1**, 204–217.
2 R. M. Tost, J. S. Gonzalez and P. M. Torres, *J. Mater. Chem.*, 2002, **11**, 3331–3336.
3 Z. B. Wu, B. Q. Jiang, Y. Liu, W. R. Zhao and B. H. Guan, *J. Hazard. Mater.*, 2007, **145**, 488–494.
4 C. C. Zhou, Y. P. Zhang, X. L. Wang, H. T. Xu, K. Q. Sun and K. Shen, *J. Colloid Interface Sci.*, 2013, **392**, 319–324.
5 E. James and I. I. Parks, *Science*, 2010, **26**, 1584–1585.
6 X. Y. Shi, F. D. Liu, L. J. Xie, W. P. Shan and H. He, *Environ. Sci. Technol.*, 2013, **47**, 3293–3298.
7 Y. Li, J. H. Peng, X. Huang, X. Li, W. K. Su, X. X. Sun, D. Z. Wang and J. M. Hao, *Environ. Sci. Technol.*, 2014, **48**, 4515–4520.
8 Q. Li, H. S. Yang, F. M. Qiu and X. B. Zhang, *J. Hazard. Mater.*, 2011, **192**, 915–921.
9 J. Li, H. Chang, L. Ma, J. Hao and R. T. Yang, *Catal. Today*, 2011, **175**, 147–156.
10 M. S. Maqbool, A. K. Pullura and H. P. Ha, *Appl. Catal., B*, 2014, **152–153**, 28–37.
11 Y. Peng, J. Li, W. Shi, J. Xu and J. Hao, *Environ. Sci. Technol.*, 2012, **46**, 12623–12629.
12 R. H. Gao, D. S. Zhang, X. G. Liu and L. Y. Shi, *Catal. Sci. Technol.*, 2013, **1**, 191–199.
13 F. D. Liu, H. He, C. B. Zhang, W. P. Shan and X. Y. Shi, *Catal. Today*, 2011, **175**, 18–25.
14 L. Chen, J. H. Li and M. F. Ge, *Chem. Eng. J.*, 2011, **170**, 531–537.
15 J. Chen, M. Shen, X. Wang, G. Qi, J. Wang and W. Li, *Appl. Catal.*, 2013, **134–135**, 251–257.
16 P. Fabrizioli, T. Burgi and A. Baiker, *J. Catal.*, 2002, **206**, 143–154.
17 M. A. Larrubia, G. Ramis and G. Busca, *Appl. Catal., B*, 2001, **30**, 101–110.

18 Y. J. Kim, H. J. Kwon, I. S. Nama, J. W. Choung, J. K. Kil, H. J. Kim, M. S. Cha and G. K. Yeo, *Catal. Today*, 2010, **151**, 244–250.
19 S. Roy, B. Viswanath, M. S. Hegde and G. Madras, *J. Phys. Chem. C*, 2008, **112**, 6002–6012.
20 Z. L. Liu, Y. Yi, S. X. Zhang, T. L. Zhu, J. Z. Zhu and J. G. Wang, *Catal. Today*, 2013, **216**, 76–81.
21 W. Tian, H. Yang, X. Fan and X. Zhang, *J. Hazard. Mater.*, 2011, **188**, 105–109.
22 Z. Chen, F. Wang, H. Li, Q. Yang, L. Wang and X. Li, *Ind. Eng. Chem. Res.*, 2012, **51**, 202–212.
23 H. Li, D. Zhang, P. Maitarad, L. Shi, R. Gao, J. Zhang and W. Cao, *Chem. Commun.*, 2012, **48**, 10645–10647.
24 J. Shan, Y. Zhu, S. Zhang, T. Zhu, S. Rouvimov and F. Tao, *J. Phys. Chem. C*, 2013, **117**, 8329–8335.
25 S. Yang, J. Li, C. Wang, J. Chen, L. Ma, H. Chang, L. Chen, Y. Peng and N. Yan, *Appl. Catal., B*, 2012, **117–118**, 73–80.
26 H. Q. He, J. Yin, Y. X. Li, Y. Zhang, H. S. Qiu and J. B. Xu, *Appl. Catal., B*, 2014, **156–157**, 35–43.
27 S. Kim and S. K. Lim, *Appl. Catal., B*, 2008, **84**, 16–20.
28 C. Wessel, R. Ostermann, R. Dersch and B. M. Smarsly, *J. Phys. Chem. C*, 2011, **115**, 362–372.
29 D. Ma, Y. J. Xin, M. C. Gao and J. Wu, *Appl. Catal., B*, 2014, **147**, 49–57.
30 S. J. Yang, C. Z. Wang, J. H. Li, N. Q. Yan, L. Ma and H. Z. Chang, *Appl. Catal., B*, 2011, **110**, 71–80.
31 X. C. Li, V. T. John, J. J. Zhan, G. H. He, J. B. He and L. Spinu, *Langmuir*, 2011, **27**, 6252–6259.
32 Y. Wan, W. Zhao, Y. Tang, L. Li, H. Wang, Y. Cui, J. Gu, Y. Li and J. Shi, *Appl. Catal., B*, 2014, **148–149**, 114–122.
33 C. R. Gong, D. R. Chen, X. L. Jiao and Q. L. Wang, *J. Mater. Chem.*, 2002, **12**, 1844–1847.
34 S. H. Zhan, J. Y. Yang, Y. Liu, N. Wang, J. J. Dai, H. B. Yu, X. C. Gao and Y. Li, *J. Colloid Interface Sci.*, 2011, **355**, 328–333.
35 G. Giecko, T. Borowiecki, W. Gac and J. Kruk, *Catal. Today*, 2008, **137**, 403–409.
36 M. R. Morales, B. P. Barbero and L. E. Cadus, *Appl. Catal., B*, 2007, **74**, 1–10.
37 C. Wang, S. Yang, H. Chang, Y. Peng and J. Li, *J. Mol. Catal. A: Chem.*, 2013, **376**, 13–21.
38 B. Thirupathi and P. G. Smirniotis, *J. Catal.*, 2012, **288**, 74–83.
39 D. A. Peña, B. S. Uphade and P. G. Smirniotis, *J. Catal.*, 2004, **221**, 421–431.
40 Y. J. Kim, H. J. Kwon, I. Heo, I. S. Nam, B. K. Cho, J. W. Choung, M. S. Cha and G. K. Yeo, *Appl. Catal., B*, 2012, **126**, 9–21.
41 Y. Shu, H. Sun, X. Quan and S. Chen, *J. Phys. Chem. C*, 2012, **116**, 25319–25327.
42 L. Chen, J. Li and M. Ge, *Environ. Sci. Technol.*, 2010, **44**, 9590–9596.
43 Y. Shu, H. Sun, X. Quan and S. Chen, *J. Phys. Chem. C*, 2012, **116**, 25319–25327.
44 M. Casapu, O. Krocher, M. Mehring, M. Nachtegaal, C. Borca, M. Harfouche and D. Grolimund, *J. Phys. Chem. C*, 2010, **114**, 9791–9801.
45 G. Ramis and M. A. Larrubia, *J. Mol. Catal. A: Chem.*, 2004, **215**, 161–167.
46 A. Karami and V. Salehi, *J. Catal.*, 2012, **292**, 32–43.
47 H. J. Chae, S. T. Choo, H. Choi and I. S. Nam, *Ind. Eng. Chem. Res.*, 2000, **39**, 1159–1170.
48 A. Shi, X. Wang, T. Yua and M. Shen, *Appl. Catal.*, 2011, **106**, 359–369.